Monthly Notices
of the
ROYAL ASTRONOMICAL SOCIETY
MNRAS **455,** 691–702 (2016) doi:10.1093/mnras/stv2319

Strong constraints on a super-Eddington accretion flow: *XMM–Newton* observations of an intermediate-mass black hole

Chichuan Jin,[1,2]★ Chris Done[3] and Martin Ward[3]

[1]*Qian Xuesen Laboratory of Space Technology, China Academy of Space Technology, Youyi Road, Beijing 100094, China*
[2]*Max Planck Institut für Extraterrestrische Physik, D-85748 Garching, Germany*
[3]*Department of Physics, University of Durham, South Road, Durham DH1 3LE, UK*

Accepted 2015 October 5. Received 2015 August 14; in original form 2015 April 23

ABSTRACT

RX J1140.1+0307 is a Narrow Line Seyfert 1 (NLS1) with one of the lowest black hole masses known in an AGN ($M \leq 10^6$ M$_\odot$). We show results from two new *XMM–Newton* observations, exhibiting soft 2–10 keV spectra, a strong excess at lower energies, and fast X-ray variability which is typical of this class of AGN. The soft excess can be equally well fit using either low-temperature Comptonization or highly smeared, ionized reflection models, but we additionally consider the fast X-ray variability to produce covariance, lag and coherence spectra to show that the low-temperature Comptonization model gives a better description of the break in variability properties between soft and hard X-rays. Both these models require an additional component at the softest energies, as expected from the accretion disc. However, standard disc models cannot connect this to the optical/UV emission from the outer disc unless the mass is underestimated by an order of magnitude. The variable optical and far UV emission instead suggests that $L/L_{\rm Edd} \sim 10$ through the outer disc, in which case advection and/or wind losses are required to explain the observed broad-band spectral energy distribution. This implies that the accretion geometry close to the black hole is unlikely to be a flat disc as assumed in the recent X-ray reverberation mapping techniques.

Key words: accretion, accretion discs – galaxies: nuclei – galaxies: Seyfert – X-rays: galaxies.

1 INTRODUCTION

Intermediate-mass black holes (IMBH), in the range 10^4–10^6 M$_\odot$, are of particular interest because this population would fall within the gap between the two principal black hole (BH) populations, i.e. supermassive black holes (SMBH) with $M \geq 10^6$ M$_\odot$ and stellar mass BHs with $M \sim 10$ M$_\odot$. Currently, there are very few well-studied IMBH. Two examples are NGC 4395 (Filippenko & Ho 2003) and POX 52 (Kunth, Sargent & Bothun 1987; Barth et al. 2004).

Over two decades, the most robust technique to measure BH masses in active galactic nuclei (AGN) has been the reverberation mapping (RM) technique, which estimates the radius of the broad-line region (BLR) by measuring the time lag between the line emission from the BLR and the intrinsic continuum emission from the accretion disc. Since optical RM requires well-sampled spectroscopic monitoring of variable AGN over months and years, the total number of sources with RM masses is currently less than 40 (e.g. Kaspi et al. 2000; Peterson et al. 2004, 2005; Denney et al. 2006; Bentz et al. 2009b; Du et al. 2014). Alternatively, the RM measurements can be used to derive a radius–luminosity relation which can then provide BH mass based on single epoch measurements using the Balmer line width (normally the FWHM of H β) and the luminosity (generally the monochromatic luminosity at 5100 Å, hereafter λL_{5100} e.g. Bentz et al. 2006, 2009a; Denney et al. 2010). By employing this method, Greene & Ho (2004) identified 19 IMBH in the Sloan Digital Sky Survey (SDSS) data base. Following this work, Dong et al. (2007) and Greene & Ho (2007) extended the IMBH sample to include several hundred sources.

RX J1140.1+0307 (hereafter RX1140), also referred to as GH 08 or SDSS J114008.71+030711.4, is amongst the original 19 IMBH sample of Greene & Ho (2004). It has a redshift of 0.081 (comoving distance of 336 Mpc). The SDSS and *Hubble Space Telescope (HST)* images show a resolved galactic disc component, plus a bar and unresolved nuclear component (Greene, Ho & Barth 2008). The FWHM of H β measured from the SDSS spectrum is 700–780 km s^{-1} (Ai et al. 2011; Jin et al. 2012a). However, to obtain a BH mass also requires λL_{5100}. Determination of this is made more difficult by the presence of contamination from the host galaxy. Deconvolution of the *HST* image gives an estimated AGN continuum of $\lambda L_{5100} \sim 6 \times 10^{42}$ergs^{-1}, which is lower than the observed variable flux of $\lambda L_{5100} \sim 8 \times 10^{42}$ergs^{-1} (Rafter et al. 2011). This gives a BH mass of 8–10 $\times$ 10^5 M$_\odot$ (Greene et al. 2008; Ai et al.

★ E-mail: chichuan@mpe.mpg.de

2011). However, Rafter et al. (2011) applied the RM technique to RX1140, and reported an upper limit of 6 light days for $R_{\rm BLR}$, which gives a BH mass of $M \lesssim 5.8 \times 10^5\,{\rm M}_\odot$, but this is probably too strong a limit noting their average sampling time of 6.1 d. A more conservative upper limit from the reverberation is probably a factor 2 larger, giving $M \lesssim 1.2 \times 10^6\,{\rm M}_\odot$, which is consistent with the H β BH mass estimate.

For this low BH mass, the total AGN luminosity is likely to be a high fraction of the Eddington value. Zhang & Wang (2006) estimate $L/L_{\rm Edd} \sim 1.6$ from $L_{\rm bol} = 9 \times \lambda L_{5100}$, but using the luminosity corrected for host galaxy contamination significantly reduces this to 0.6. Such high (super) Eddington fraction accretion flows, with $L/L_{\rm Edd} \gtrsim 1$, are found in a subset of broad-line AGN known as Narrow-Line Seyfert 1 (NLS1; e.g. Osterbrock & Pogge 1985; Boroson & Green 1992; Leighly 1999). Their narrow width Balmer lines suggest relatively low BH masses ($10^{6-7}\,{\rm M}_\odot$: Boroson 2002), and so their bolometric luminosities are close to Eddington. For such high Eddington fractions, it remains an open question as to whether the H β scaling relations still apply. Marconi et al. (2009) suggest that a correction to the BH mass scalings is needed because the BLR clouds trace the effective gravity. But the lack of observed wind features in the low-ionization BLR lines provides a strong argument against such effects being important. This could indicate that the clouds are optically thick to electron scattering, with columns of $>10^{24}$ cm^{-2}, or that the radiative acceleration only affects the front face of the cloud (Baskin, Laor & Stern 2014). Therefore, it seems probable that the H β line widths track the BH mass up to the Eddington limit and possibly beyond.

One of the ubiquitous features of high Eddington fraction AGN is their prominent soft X-ray excess superposed on a steep X-ray power law which is very variable. These properties are observed in the X-ray spectrum of RX1140 (Miniutti et al. 2009; Ai et al. 2011). Since the variability scales with BH mass, it is not surprising that the X-ray variability of RX1140 is amongst the strongest seen in AGN (e.g. Ponti et al. 2012; Ludlam et al. 2015). However, the origin of the soft excess is more puzzling. Models which can reproduce its energy distribution include optically thick, low-temperature Comptonization (e.g. Laor et al. 1997; Magdziarz et al. 1998; Gierliński & Done 2004; Jin et al. 2013), ionized, highly smeared reflection (e.g. Fabian & Miniutti 2005; Zoghbi et al. 2010; Fabian et al. 2013; Fabian, Kara & Parker 2014; Uttley et al. 2014), and smeared absorption (Gierliński & Done 2004, 2006). The smeared absorption model is not favoured on either theoretical (Schurch & Done 2007) or observational grounds (Miniutti et al. 2009, Ai et al. 2011), but both Comptonization and smeared reflection provide a good fit to the soft excess in this object (Ai et al. 2011).

However, for such low BH mass, high-mass accretion rate AGN, the disc itself should also contribute a significant fraction of the emission in the soft X-ray bandpass. It is well known that the accretion flow spectrum is not well described by a disc in standard broad-line Seyfert 1s and Quasars (e.g. Elvis et al. 1994). But the higher Eddington ratio NLS1 have spectra that do appear to be more disc dominated (Jin et al. 2012a; Jin, Ward & Done 2012c; hereafter J12a,b; Done et al. 2012, hereafter D12). This is most clearly understood in the context of the full spectral energy distribution (SED), as the optical/UV disc normalization is determined by the product of BH mass and mass accretion rate, with $L_\nu \propto (M\dot{M})^{2/3}$. So this directly measures the mass accretion rate provided the BH mass is known, and hence the total luminosity $L = \eta \dot{M} c^2$, where the efficiency η depends on the BH spin (e.g. Davis & Laor 2011; Done et al. 2013). This also predicts where the disc emission should peak, and shows that the disc spectrum should extend to soft X-ray energies for the NLS1, even if they have low spins (Done et al. 2013).

RX1140 has the lowest BH mass of all the 12 NLS1s included in the sample of 51 unobscured type 1 AGN of J12a,b. These papers reported a detailed study of the broad-band SED from optical to hard X-rays, fitting them with a new accretion disc model which conserves the total accretion energy by dissipating some of it into the Comptonized soft X-ray excess and the power-law tail, with the rest being emitted by the thin disc (D12). The consequence of energy conservation within these components is that there is no strong energy loss via advection and/or winds as might be expected in highly super-Eddington sources. J12a,b took the BH mass as a fit parameter within the uncertainties derived from using the intermediate and broad H β line component widths as lower and upper limits, respectively. This gave a best-fitting value of $2.9 \times 10^6\,{\rm M}_\odot$(J12a), which increased to $6 \times 10^6\,{\rm M}_\odot$ when the updated SED model, which included a term for colour temperature correction to the disc emission, were used (D12, J12b). It can be seen that the BH mass of RX1140 derived from broad-band SED fitting is much higher than the virial and RM BH mass estimates, and this fact requires further consideration.

The X-ray properties of RX1140 are very similar to a small group of the most extreme NLS1s, including PG 1244+026, RE J1034+396 and RX J0136.9-3510, all of which exhibit strong X-ray variability, prominent and featureless soft excesses, and are all reported to be accreting close to the Eddington limit (Middleton et al. 2009; Jin et al. 2009, 2013). In order to investigate the physical interpretation for the soft excess seen in RX1140, detailed timing analysis and spectral analysis should be performed simultaneously (e.g. Jin et al. 2013). To achieve this, we applied for a long *XMM–Newton* observation for this source. This application was successful, but it was split into two observations separated by two weeks. In this paper, we present the results from a combined analysis of these two new*XMM–Newton* observations, plus the previous one extracted from the archive.

This paper is organized as follows: Section 2 describes the data reduction procedures used for the *XMM-Newton* observations. Section 3 presents the variability properties of RX1140. Section 4 presents a combined spectral and variability study. We then compare two physical models to explain the properties of the 0.3–10 keV X-ray spectra and the X-ray variability. In Section 5, we perform broad-band SED fitting by including ultraviolet (UV), optical and near-infrared data. In Section 6, we discuss related issues such as various estimates of the BH mass, UV/optical luminosity and the mechanism responsible for the soft X-ray excess. Our summary and conclusions are given in Section 7. When converting flux to luminosity, we adopt a flat universe model with the Hubble constant $H_0 = 72$ km s^{-1} Mpc^{-1}, $\Omega_{\rm M} = 0.27$ and $\Omega_\Lambda = 0.73$.

2 DATA REDUCTION

RX1140 was observed by the *XMM–Newton* satellite on the 2005 December 3 (Principal Investigator: Dr Giovanni Miniutti) (hereafter: Obs-1). We proposed a longer observation with the aim to study its X-ray variability. Our observation was divided into two parts due to satellite scheduling. These were carried out on the 2013 December 18 (hereafter: Obs-2) and on the 2014 January 1 (hereafter: Obs-3). During these three observations, the EPIC cameras were in the full window mode. We used SAS v13.5.0 and the latest calibration files, and followed the standard procedures to reduce the data. We defined the source extraction region to be a circular region of radius 45 arcsec for each EPIC camera. The background

was selected from a nearby circular region with the same radius as for the source. For Obs-1, the net source count rates are 0.62, 0.13 and 0.13 ct s^{-1} for the PN, MOS1 and MOS2, respectively. Obs-2 has a mean count rate that is half that of Obs-1. Obs-3 has a similar mean count rate as Obs-1. All of these count rates are well below the threshold count rates capable of causing photon pile-up effects when using the full window mode of the EPIC cameras.

We selected data with PATTERN ≤ 12 for MOS1 and MOS2, and PATTERN ≤ 4 for the PN. Light curves were extracted from both the source and background regions. There were high-background flares during all three observations. Therefore, we visually checked the background light curves to identify high-background sections and removed them. Then the background was subtracted from the source light curve using LCMATH in FTOOLS. Spectra were extracted for the source and background regions, separately. Response matrices were produced using RMFGEN and ARFGEN. Areas for the source and background regions were calculated using BACKSCALE. We also used the SAS task RGSPROC to extract the first-order spectra from RGS1 and RGS2. Response matrices for the RGS were produced with RGSRMFGEN. All spectra were rebinned by GRPPHA with a minimum of 25 counts per bin, so that the χ^2 fitting is appropriate. But the signal to noise of RGS spectra is too low to provide further information, so we do not present them in this paper. All spectral fittings were performed in XSPEC v12.8.2 (Arnaud 1996).

There are simultaneous optical/UV observations obtained using the *XMM–Newton* optical monitor (OM). OBs-1 has *UVW*1 and *UVM*2 filter data, while Obs-2 and 3 have *U*, *B* and *UVW*1. We searched the OM source list file to obtain the count rate of RX1140, in each available filter, and inserted these values into the standard OM data file template *om_filter_default.pi*.[1] The data file was then combined with the 'canned' response files to be ready for XSPEC fitting.

3 THE VARIABILITY STUDY

The background-subtracted PN light curves over the total energy band (0.3–10 keV) are shown in Fig. 1. Strong variability is observed on all time-scales. This is confirmed by inspection of the power spectral density (PSD) in Fig. 2. The flat PSD indicates that intrinsic variability (i.e. Poisson noise subtracted) exists across the 0.2–10 ks time-scale. None of the observations show any sign of a high-frequency break. This is clearly different from the case of PG 1244+026, where the 0.3–1 keV power spectrum drops substantially above $\sim 10^{-3}$ Hz (Jin et al. 2013), strongly suggesting that RX1140 has a substantially lower BH mass than PG 1244+026, and that the BH mass is around $\lesssim 10^6$ $M_\odot$ (Ponti et al. 2012; Kelly et al. 2013; Ludlam et al. 2015).

The upper panel of Fig. 3 a shows the time-averaged spectrum of Obs-1 (black). The fast variability seen in Fig 1a does not significantly change the spectral shape. We select based on intensity to construct a high ($pn\_rate \geq 0.7$ ct s^{-1}: orange) and low ($pn\_rate \leq 0.35$ ct s^{-1}: blue) count rate spectra from Obs-1. These are identical within errors to the mean spectrum. This can be seen in the lower panels of Fig. 3a, which gives the ratio of each data set to the mean spectral model, renormalized to the 2–10 keV count rate.

Over longer time-scales, the spectral shape does change. The upper panel of Fig. 3 b compares the time-averaged X-ray spectra for Obs-1 (black) and Obs-2 (red). The mean spectrum of Obs-3 is almost identical to Obs-1, and so it is not shown in the figure. A ratio of the best-fitting model to Obs-1 (black solid model) rescaled to the observed 2–10 keV spectrum of Obs-2 (red solid model) significantly underpredicts the soft emission, as can be seen also in the lower panel which gives the ratio of each data set to the model.

[1] http://heasarc.gsfc.nasa.gov/FTP/xmm/data/responses/om

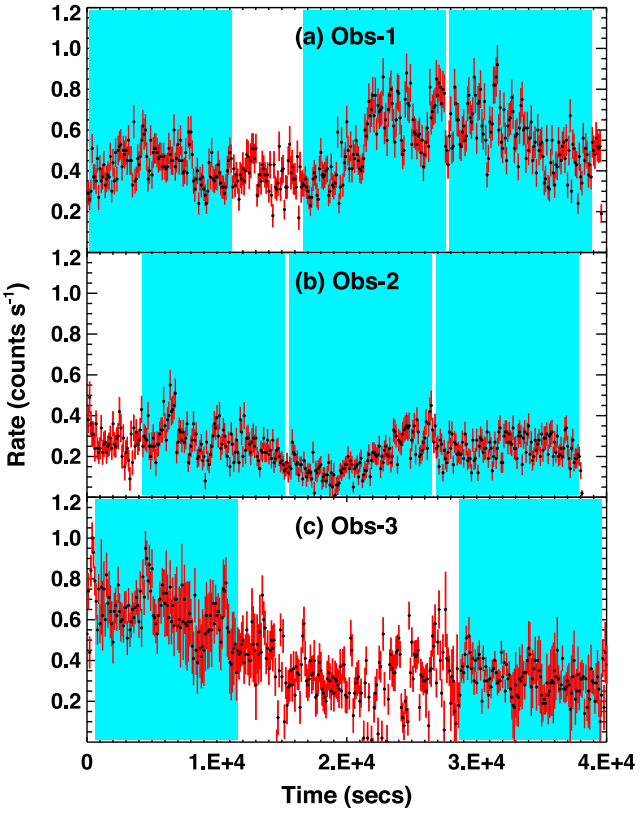

Figure 1. The 100 s binned, background subtracted, 0.3–10 keV light curves for Obs-1, Obs-2 and Obs-3. Each cyan region is a 11 ks segment that is free from high-background contaminations.

3.1 The RMS Spectra

The fractional variability observed in different energy bins, i.e. the RMS spectra (e.g. Edelson et al. 2002; Markowitz, Edelson & Vaughan 2003; Vaughan et al. 2003), can be very useful in decomposing the different spectral components. We use the segment algorithm described in Wilkinson & Uttley (2009) to calculate the RMS. For every energy bin, the light curve is divided evenly into several segments. Then the excess variance is calculated for every segment and averaged over all segments. The square root of the excess variance is the RMS. The error bars are calculated using equation B2 in Vaughan et al. (2003). The binning time and segment length determine the time-scale for which the RMS is calculated. The occurrence of intervals of high-background interrupt the continuity of the light curve. In Obs-3, the longest continuously sampled segment is only 11 ks, whereas it is longer in Obs-1 and Obs-2. In order to mitigate any bias introduced by high-background contamination, we choose a longest time segment of 11 ks, and we can identify a total of eight segments all with little high background, i.e. three segments in Obs-1, three in Obs-2 and two in Obs-3 (see the cyan regions in Fig. 1).

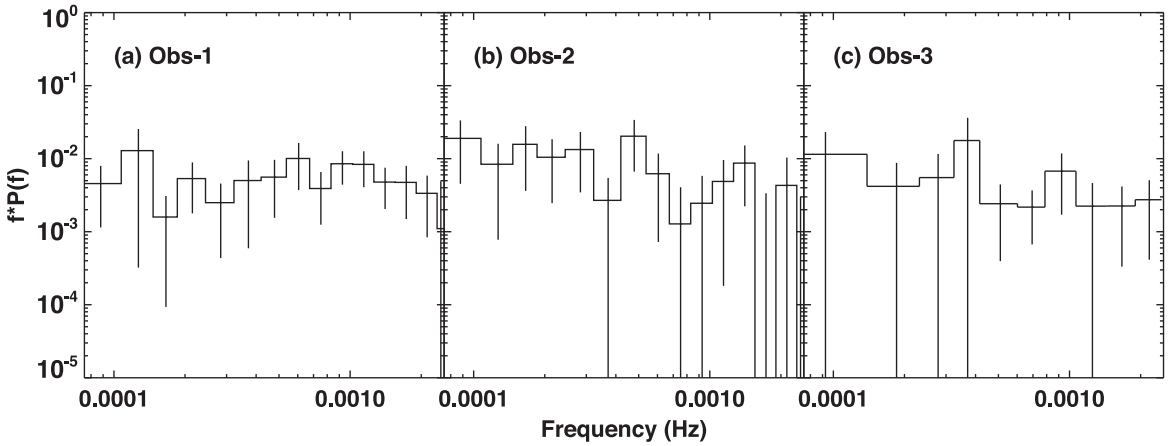

Figure 2. PSD for the 0.3–10 keV light curves of the three observations obtained using FTOOL powspec after subtracting the Poisson counting noise. For Obs-3, only the two 11 ks segments in Fig. 1 were used to avoid the influence of high background.

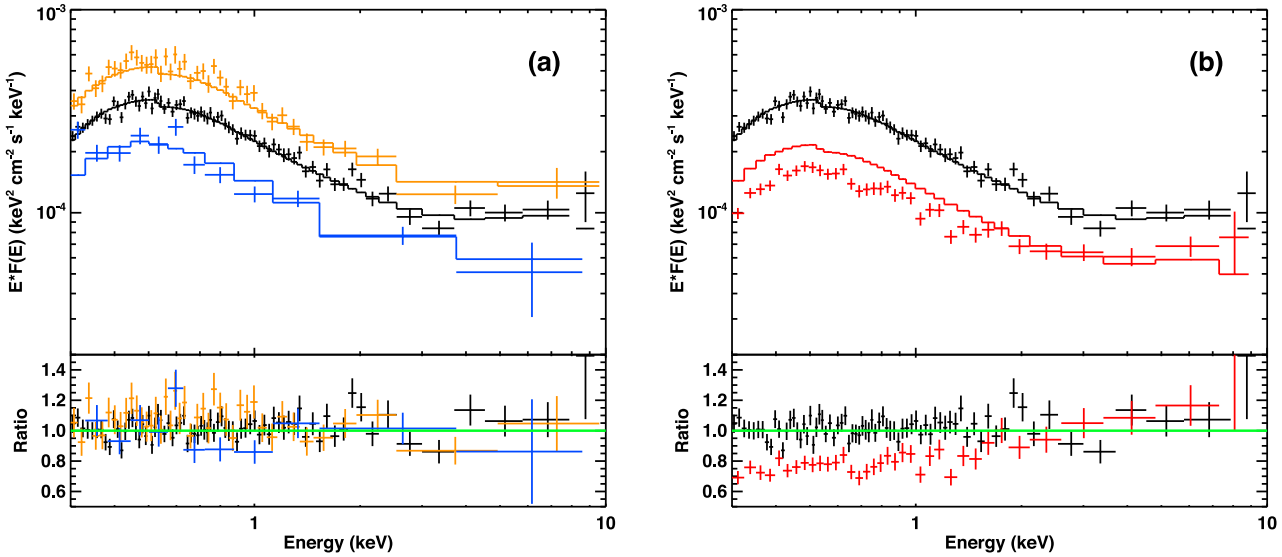

Figure 3. Panel a: time-averaged spectra of Obs-1 (black), together with the high count rate ($pn\_rate \geq 0.7\,\mathrm{ct\,s^{-1}}$: orange) and low count rate ($pn\_rate \leq 0.35\,\mathrm{ct\,s^{-1}}$: blue) spectra seen within Obs-1. The best-fitting model of Obs-1 is the same as in Fig. 5a, then renormalized to match the 2–10 keV of each spectrum. The lower panel shows the ratio of each data set to the model. Panel b: time-averaged spectra of Obs-1 (black) and Obs-2 (red), there is significant spectral variability in Obs-2, where the soft X-rays are weaker.

There are insufficient data to produce frequency-resolved RMS spectra. Instead, we calculate only *RMS* of the high-frequency (HF) variability using time-scales of 0.2–2 ks extracted from those eight segments. The results are shown in Fig. 4. Interestingly, the HF RMS spectra reveal a rising shape from the soft to hard X-ray ranges in Obs-1 and Obs-3. This is similar to that observed in some other high-mass accretion rate NLS1s, such as PG 1244+026 (Jin et al. 2013), RE J1034+396 (Middleton et al. 2009) and RX J0136.9−3510 (Jin et al. 2009). This difference in variance between soft and hard energy bands can be explained if the soft X-ray excess varies less than the power-law tail, so favouring models where this is a true additional component e.g. from soft Comptonization (e.g. Gierliński & Done 2004, Middleton et al. 2009, Jin et al. 2013, Matt et al. 2014) rather than due to ionized, smeared reflection, as this tends to contribute equally in the soft and hard bands (Gierliński & Done 2006).

Another important feature seen in Fig. 4 is that the 0.3–1 keV HF RMS in Obs-2 is rather different to what is seen in Obs-1 and Obs-3, with much less difference between the fast variability as a function of energy (more HF power below 1 keV, and marginally less at the highest energies). Whatever process occurred to depress the soft spectrum relative to the mean (Fig. 3b) may also have increased its fast variability (see Gardner & Done 2015 for a possible explanation of this in terms of cloud occlusion in the inner disc).

3.2 The covariance spectra

The RMS variability spectrum shows all variability at each energy, but there may be multiple components. A more powerful technique is to produce a covariance spectrum (developed by Wilkinson & Uttley 2009), as this determines the spectrum of the variability correlated with a given energy band light curve used as a reference. For the NLS1 PG 1244+026, Jin et al. (2013) showed that using the fastest variability observed in the hard X-ray (2–10 keV) light curve as a reference band, gave strong evidence for a Comptonization origin for the soft X-ray excess, while using the fastest variability

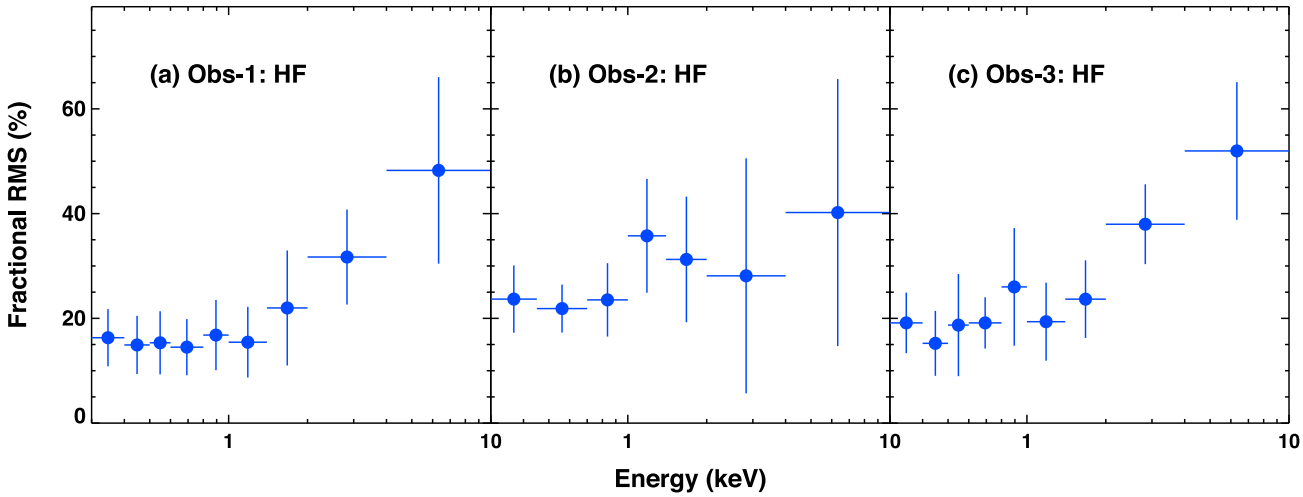

Figure 4. The HF (0.2–2 ks) RMS spectra for the three observations. Obs-1 and Obs-3 have similar fast spectral variability as well as similar mean spectra, while Obs-2 has more fast variability at low energies than both Obs-1 and Obs-3.

observed in the 0.3–1 keV band showed evidence for a contribution at the lowest energies from the disc.

Here we apply the same technique to our data sets to produce the HF (0.2–2 ks) covariance spectra using hard (2–10 keV) and soft (0.3–1 keV) X-rays as the reference band. We use only the PN detector data so as not to introduce differences in the responses from combining data from the PN and MOS. The data quality means that the signal to noise of the covariance spectra for RX1140 is much lower than for PG 1244+026. Then we study both the covariance spectra and the time-averaged spectrum (see Fig. 5) in order to constrain the origin of the soft excess, i.e. whether it can be better fit by an additional Comptonization model or by relativistically smeared reflection, and whether there is an additional contribution from the accretion disc itself.

4 SPECTRAL ANALYSIS

The X-ray spectrum derived from Obs-1 has been analysed previously by Miniutti et al. (2009). They found that an X-ray reflection plus a thermal disc model gives a better fit than the smeared absorption model. Ai et al. (2011) found that reflection and Comptonization models gave comparably good fits, and that both of these were better than smeared absorption and p-free disc models. The shape of the HF RMS and mean spectra in Fig. 3 and Fig. 4 also indicates that RX1140 may be similar to other extreme NLS1s such as PG 1244+026, RE J1034+396 and RX J0136.9−3510, whose soft X-ray excess can be well interpreted using the Comptonization model. Therefore, we try fitting both the Comptonization and reflection models for the Obs-1 and Obs-2 spectra. The time-averaged spectrum of Obs-3 is identical to that of Obs-1, but Obs-1 has better data quality than Obs-3 because of its lower background. Therefore, we only present spectra extracted from Obs-1 and Obs-2. The best-fitting models are shown in Fig. 5.

4.1 Comptonization model

For the Comptonization scenario, we use a low-temperature, optically thick Comptonization model (`comptt` model, Titarchuk 1994; Hua & Titarchuk, 1995; Titarchuk & Lyubarskij 1995) to fit the soft X-ray excess; a high-temperature Comptonization (`nthcomp` model in XSPEC, Zdziarski, Johnson & Magdziarz 1996; Życki, Done & Smith 1999) to fit the power-law tail, together with its neutral, smeared reflection (`kdblur*pexmon`, Laor 1991; recoded as a convolution model, Nandra et al. 2007). We also include an accretion disc component (`diskbb` model, Mitsuda et al. 1984; Makishima et al. 1986). Using the equation in Peterson (1997) and assuming $r_{\rm in} = 6r_{\rm g}$, Log(M) = 5.77 and $L/L_{\rm Edd} = 2.69$ (Miniutti et al. 2009), we calculate the temperature at the inner radius ($T_{\rm in}$) to be 110 eV. Including a colour temperature correction would increase this, while allowing for some of the inner disc power to be dissipated into the soft and hard X-ray Compton components would decrease it, so we freeze the parameter $T_{\rm in}$ at this temperature. This also serves as the temperature of the seed photons for both soft and hard X-ray Comptonization components. We fix the Galactic column at $N_{\rm H} = 1.91 \times 10^{20}$ cm^{-2} (Kalberla et al. 2005) but allow for some additional free absorption by a gas column in the host galaxy (`zwabs`, Morrison & McCammon 1983). The parameters for the complete XSPEC model are given in Table 1.

While there is some degeneracy between the disc and soft Comptonization components, the presence of a disc component is strongly favoured by this model when fitting the data. In the 0.3–10 keV band, stepping the disc normalization down to zero changes χ^2_υ from 0.95 to 1.00, and gives $\Delta\chi^2 = 17$ for one free parameter (note: the disc temperature is fixed in the model). In the 0.3–0.5 keV band (consisting of 37 spectral bins), the same test changes χ^2_υ from 1.26 to 1.44, and gives $\Delta\chi^2 = 7$ for one free parameter.

The HF variability is likely to originate mainly from the inner regions of the flow, where the hard X-ray emission is produced. Hence, we expect that the spectrum correlated with the HF 2–10 keV variability should have the same shape as the high-temperature Comptonization component which dominates the 2–10 keV spectrum in this model. However, reflection (and associated thermal reprocessing which could contribute to the soft X-ray excess: Gardner & Done 2015), should also vary in a correlated manner as the expected reverberation time-scale (Fabian et al. 2009) is short for a low-mass BH. Only the disc component is not expected to show any variability on these time-scales.

To perform spectral fitting, we first applied the spectral model to the entire 0.3–10 keV spectrum, but we found some parameters were not well constrained because of parameter degeneracy. Therefore, we attempt to constrain the hard X-ray Comptonization and neutral reflection components by applying them only to the 2–10 keV

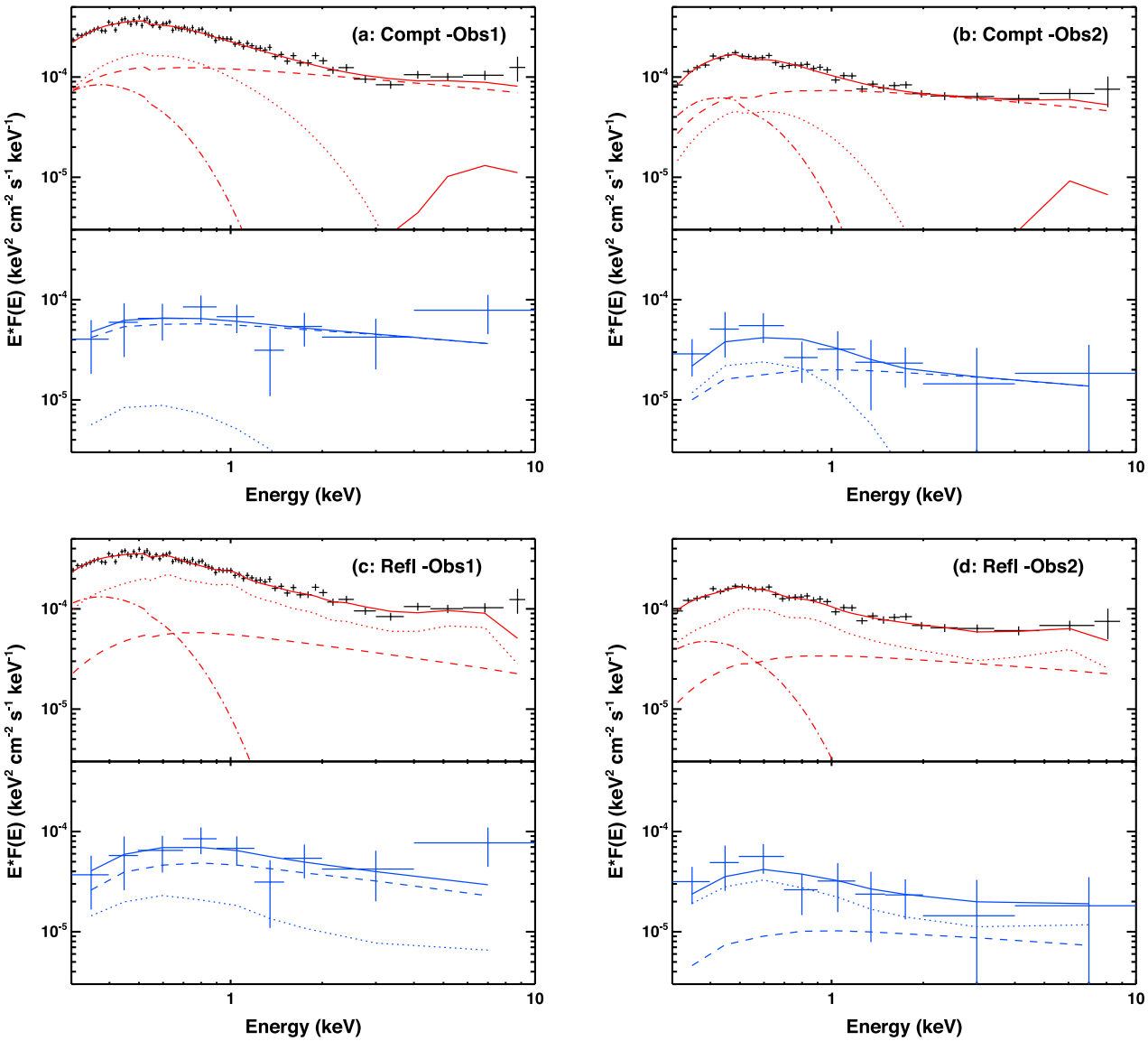

Figure 5. X-ray spectral fitting of Obs-1 (Panel Compt-Obs1, Refl-Obs1) and Obs-2 (Panel Compt-Obs2, Refl-Obs2). The upper row shows the results of Comptonization fitting to the mean (red) and HF covariance (blue) spectra. In each panel, red solid line is the best-fitting model, red dashed line is the hard X-ray Comptonization component, red dotted line is the soft X-ray Comptonization component, red dash–dotted line is the hot accretion disc component. The blue lines are spectral fits to the HF covariance spectra with only the soft and hard Comptonization components. The lower row panels present the results of reflection model fitting. The red dashed line is the intrinsic hard Comptonization component, the red dotted line is the reflected component by accretion disc, the red dash–dotted line is the accretion disc component. The blue lines are spectral fits to the covariance spectra with only the hard Comptonization and reflection components.

spectra of Obs-1 and Obs-2. The model fits the 2–10 keV spectra well ($\chi^2_v = 84/82$). The hard X-ray photon index (Γ) is found to be 2.26 $\pm$0.12, the inner radius parameter ($R_{\rm in}$) of `kdblur` is 20^{+380}_{-18} with reflection solid angle $\Omega/2\pi$ fixed at unity. Removing the neutral reflection component leads to $\Gamma = 2.13 \pm 0.12$, but the fitting statistics are only slightly worse ($\chi^2_v = 96/84$). The low signal to noise in the hard X-ray band cannot constrain this reflection component well. Then we refit the model to the entire 0.3–10 keV band by fixing Γ at 2.26 and $R_{\rm in}$ at 20, and all spectral components are better constrained than before. The best-fitting parameters are listed in Table 1.

In Obs-1, the HF covariance spectrum can be well fitted by the hard Comptonization with $\Gamma = 2.26$, without significant contribution from a variable soft Comptonization component. On the contrary, the HF covariance spectrum in Obs-2 is softer and so requires more contribution from the soft Comptonization (Fig. 5a and b). Neither covariance spectrum requires any disc component.

4.2 The reflection model

Ionized, strongly smeared disc reflection plus a thermal accretion disc component was previously claimed to be a good model for the time-averaged Obs-1 spectrum of RX1140 (Miniutti et al. 2009; Ai et al. 2011). Thus, we use `diskbb+nthcomp+kdblur*nthcomp` as our spectral model, with $T_{\rm in}$ of the disc component fixed at 110 eV as before. Fig. 5c and d shows this model applied to Obs-1 and Obs-2, respectively. Again, the low statistics mean that some parameters cannot be well

Table 1. The XSPEC model and the best-fitting parameters in Fig. 5. The upper and lower limits are the 90 per cent confidence range.

Model name	Model expression in XSPEC v12.8.2			
Comptonization	CONSTANT*WABS*ZWABS*(DISKBB+ NTHCOMP + COMPTT + KDBLUR*PEXMON)			
Spectrum	Component	Parameter	Value	Value
			Obs-1	Obs-2
Mean Spec	ZWABS	$N_{\rm H}$ (10^{22} cm^{-2})	$0\ ^{+0.82}_{-0}$	$0.027\ ^{+0.014}_{-0.015}$
	DISKBB	$T_{\rm in}$ (keV)	0.11 fixed	0.11 fixed
	DISKBB	Norm	$135\ ^{+59}_{-53}$	135 fixed
	NTHCOMP	Γ	2.26 fixed	2.26 fixed
	NTHCOMP	k$T_{\rm seed}$ (keV)	Tied to $T_{\rm in}$	Tied to T_{in}
	NTHCOMP	k$T_{\rm e}$ (keV)	100 fixed	100 fixed
	NTHCOMP	Norm	$(1.26\ ^{+0.10}_{-0.11})\times 10^{-4}$	$(8.11\ ^{+0.57}_{-0.80})\times 10^{-5}$
	COMPTT	k$T_{\rm seed}$ (keV)	Tied to $T_{\rm in}$	Tied to T_{in}
	COMPTT	kT (keV)	$0.38\ ^{+0.61}_{-0.12}$	$0.21\ ^{+1.14}_{-0.07}$
	COMPTT	τ	$10.9\ ^{+6.6}_{-5.8}$	$19.2\ ^{+15.4}_{-17.2}$
	COMPTT	Norm	$(2.68\ ^{+1.05}_{-1.66})\times 10^{-3}$	$(1.81\ ^{+1.30}_{-1.68})\times 10^{-3}$
	KDBLUR	$R_{\rm in}$ ($R_{\rm g}$)	20 fixed	20 fixed
	PEXMON	Rel$_{\rm refl}$	-1.0 pegged	-1.0 pegged
Cov. Spec	NTHCOMP	Norm	$(5.86\ ^{+1.41}_{-1.73})\times 10^{-5}$	$(2.21\ ^{+1.61}_{-1.67})\times 10^{-5}$
	COMPTT	Norm	$(1.45\ ^{+4.77}_{-1.43})\times 10^{-4}$	$(9.74\ ^{+12.81}_{-9.74})\times 10^{-4}$
		χ^2_ν	$298/314 = 0.95$	$176/224 = 0.78$
Reflection	CONSTANT*WABS*ZWABS*(DISKBB + NTHCOMP + KDBLUR*RFXCONV*NTHCOMP)			
Spectrum	Component	Parameter	Value	Value
			Obs-1	Obs-2
Mean Spec	ZWABS	$N_{\rm H}$ (10^{22} cm^{-2})	$0\ ^{+0.02}_{-0}$	$0.006\ ^{+0.031}_{-0.005}$
	DISKBB	$T_{\rm in}$ (keV)	0.11 fixed	0.11 fixed
	DISKBB	Norm	$211\ ^{+38}_{-136}$	$83\ ^{+117}_{-86}\times 10^{-4}$
	NTHCOMP	Γ	$2.42\ ^{+0.07}_{-0.11}$	$2.22\ ^{+0.10}_{-0.12}$
	NTHCOMP	Norm	$5.72\ ^{+3.80}_{-4.00}\times 10^{-5}$	$3.60\ ^{+3.00}_{-2.77}\times 10^{-5}$
	KDBLUR	Index	5 fixed	5 fixed
	KDBLUR	$R_{\rm in}$ ($R_{\rm g}$)	$4.98\ ^{+4.30}_{-2.53}$	$3.05\ ^{+1.30}_{-3.05}$
	RFXCONV	Rel$_{\rm refl}$	$-2.19\ ^{+1.14}_{-\infty}$	$-2.29\ ^{+1.61}_{-\infty}$
	RFXCONV	Fe$_{\rm abund}$	$1.39\ ^{+2.50}_{-0.71}$	$0.81\ ^{+0.84}_{-0.81}$
	RFXCONV	log ξ	$3.37\ ^{+0.37}_{-0.22}$	$2.86\ ^{+0.30}_{-0.45}$
Cov. Spec	NTHCOMP	Norm	$4.90\ ^{+3.53}_{-3.57}\times 10^{-5}$	$1.08\ ^{+1.97}_{-0.63}\times 10^{-5}$
	RFXCONV	Rel$_{\rm refl}$	$-0.28\ ^{+\infty}_{-\infty}$	$-2.60\ ^{+2.40}_{-\infty}$
		χ^2_ν	$295/312 = 0.95$	$170/222 = 0.77$

constrained. We choose to fix the illumination index of the smeared reflection at 5, and fit for the inner disc radius. This is always small in this model, at $\sim$3–5$R_{\rm g}$, so any reverberation time-scale should be short. Hence, both the high-temperature Comptonization and its reflection should vary together. However, the relatively flat HF covariance spectrum in Obs-1 favours a smaller reflection component contribution than in the time-averaged spectrum, while the softer HF covariance spectrum in Obs-2 favours a larger reflection contribution. But again the poor signal to noise means that this is not very significant (Table 1). Similar to what was found using the Comptonization soft excess fits, the accretion disc component is not detected in the HF covariance spectra.

4.3 The lag and coherence spectra

Both Comptonization and reflection models for the soft X-ray excess can give comparably good fits to both the time-averaged and HF covariance spectra. Both models also require that there is an additional soft component, which we can interpret as direct disc emission, emerging at the softest energies.

We can also use spectral coherence and time lags to constrain the X-ray spectral mechanisms (e.g. McHardy et al. 2004; Fabian et al. 2009). However, the low count rate of RX1140 and the relatively short continuously sampled light-curve segments ($\lesssim$11 ks, see Section 3) mean that the statistics are limited. We calculate these following Nowak et al. (1999), using only Obs-1 and 3 (since Obs-2 has a significantly different spectrum and variability). We choose a low- and a high-energy band, with 0.3–0.7 and 1.8–2.5 keV, respectively, to best distinguish the different spectral components whilst still containing enough counts.

Fig. 6 a shows that there is a soft reverberation lag of $\sim$200 s seen between the 0.3–0.7 and 1.8–2.5 keV light curves at a frequency of $\sim 2 \times 10^{-3}$ Hz. But the zero spectral coherence and the dominance of Poisson noise at this frequency means this lag could be spurious. There is however a clear positive lag at the lowest frequencies (below 2×10^{-4} Hz), where the soft leads the harder band. This lag is supported by the good spectral coherence between these bands up to 6×10^{-4} Hz (Fig. 6c and d). We note that Poisson noise will not be an issue over such long time-scales. Fig. 6b shows the energy spectrum of this long time-scale soft lead, showing that there is a clear break between the time lags at low and high energy, although the statistics are poor at hard X-ray energies. This feature is not easily compatible with the reflection model shown in Fig. 5b, where a single component dominates the spectrum from 0.4 to 10 keV.

Thus, while the low signal to noise is a problem, these data provide marginal evidence, in terms of spectral coherence and time lag, to support a model in which the bulk of the soft X-ray excess does

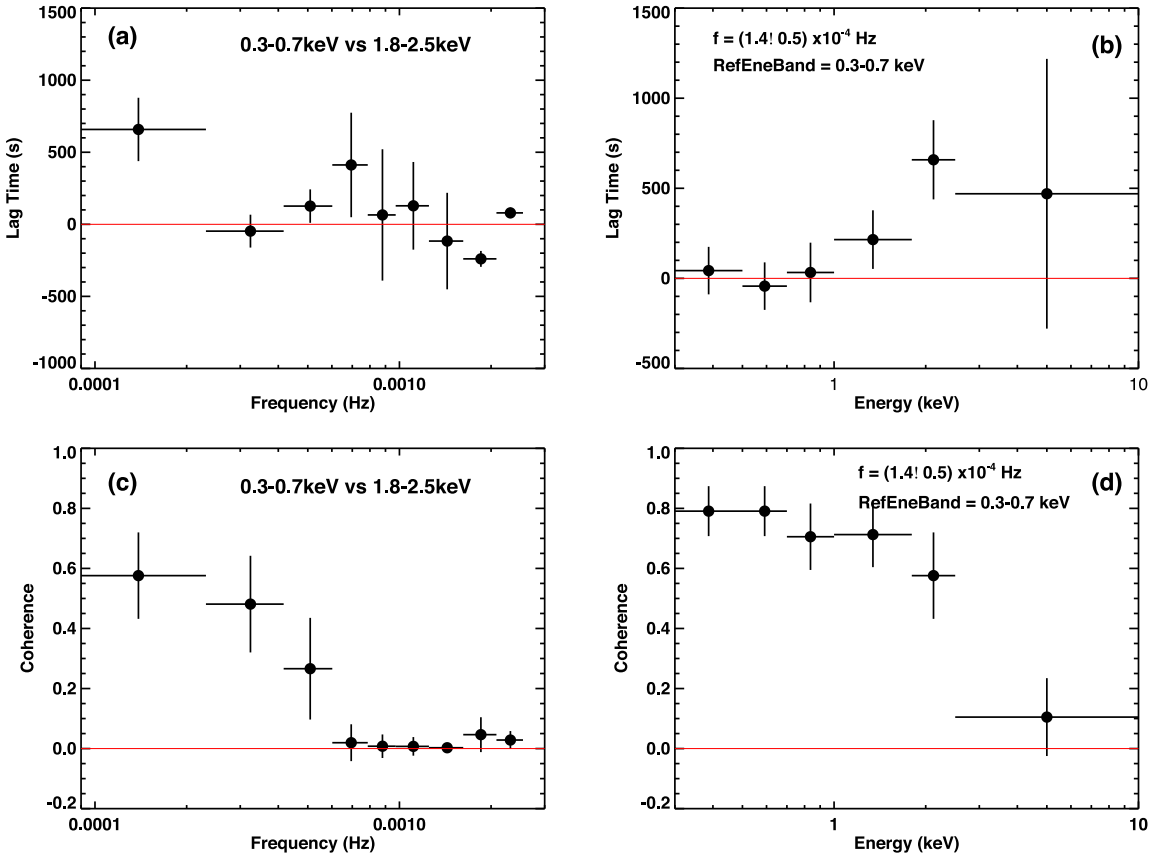

Figure 6. Frequency and energy resolved time lag and coherence for RX1140. The points are derived from five segments of 11 ks length each, which comprise three segments in Obs-1 and two segments in Obs-3 (see Section 3).

not contribute to emission over the 2–10 keV bandpass, so favouring the low-temperature Comptonization origin over the reflection dominated model.

5 BROAD-BAND SED

5.1 Multiwavelength Data

As outlined in the introduction, RX1140 was reported as an IMBH, whose mass is estimated to be 5–10 $\times$ 10^5 $M_\odot$ accreting at a high fraction of the Eddington limit. We construct a multiwavelength SED based on non-simultaneous observations (Fig. 7). We use the *XMM–Newton* PN spectrum from Obs-1 taken in 2005, together with archival data from the *ROSAT* PSPCB (1992-06-16) which we reduced using XSELECT v2.4b. The spectra were regrouped fixing a minimum of 25 counts per bin, and are in good agreement with the time-averaged PN *XMM–Newton* spectrum.

In the optical and UV band, there are simultaneous photometric points from *XMM–Newton* OM for Obs-1 (*UVM*2 and *UVW*1 filters) and Obs-2 and Obs-3 (*UVW*1, *U* and *B* filters). The *UVW*1 filter fluxes of Obs-1 and Obs-3 are very similar, so are their X-ray fluxes, so we use all OM data from these two observations (except for *UVW*1 since its waveband is already covered by the combination of *UVM*2, *U* and *B* filter bands). We do not use Obs-2 because it is clearly different in the optical/UV as well as X-ray, with only 90 per cent flux in *UVW*1, 84 per cent in *U* and 99 per cent in *B* compared to Obs-3. These are less suppressed than the X-ray flux (Obs2/Obs3 = 46 per cent in 0.3–2 keV, 63 per cent in 2–10 keV),

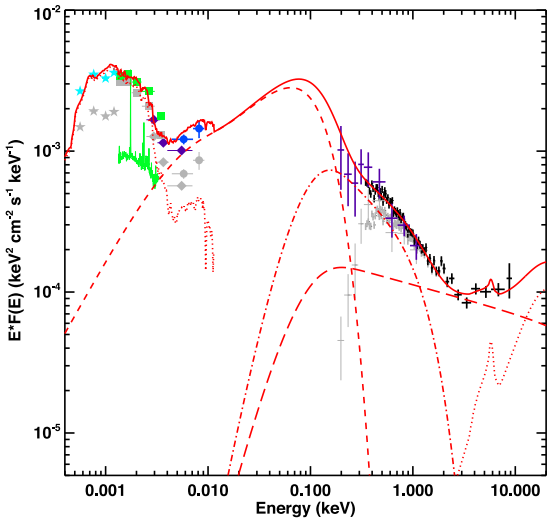

Figure 7. Broad-band SED of RX1140. Black data in the X-ray band is the Obs-1 mean spectrum, purple data in the soft X-ray band is from *ROSAT*. The UV, optical, infrared photometric points comprise *GALEX* (blue circles), OM of *XMM–Newton* (purple diamonds), SDSS UGRIZ (green squares) and fibre (green spectrum), *UKIDSS* JYHK (cyan stars). The original data before any correction are plotted in grey. The best-fitting `optxagnf` model assuming BH mass as a free parameter is shown as a red solid line is the best-fitting model, which includes host galaxy (dot line in the IR/optical), accretion disc (short dashed line), soft X-ray Comptonization (dash–dotted line), hard X-ray Comptonization (long dashed line) and a distant reflection (dot line in the hard X-ray). This best-fitting model gives $M \sim 10^7$ $M_\odot$.

indicating that the amplitude of UV/optical variability is less than that of the X-ray over variability time-scales of weeks and years.

Other data points in Fig. 7 include *GALEX* photometry (obs-date: 2007-03-22), SDSS UGRIZ PSF photometry and fibre spectrum (obs-date: 2001-03-26), *UKIDSS* Petrosian magnitude of JYHK photometry (obs-date: 2008-04-21). The difference in the normalization, especially that between the *UKIDSS*, SDSS fibre fluxes and UGRIZ points, is most likely due to different aperture sizes. We only show the SDSS fibre spectrum for completeness, and do not include these data in the broad-band SED fitting.

5.2 Broad-band SED fitting

We use `optxagnf` in XSPEC v12.8.2, to fit the SED from the optical to hard X-ray energies (D12). This includes both intrinsic disc emission and low- and high-temperature Comptonization, as favoured by the spectral fits in Section 4. An additional neutral reflection (`kdblur*pexmon` model, Laor 1991, recoded as a convolution model by Nandra et al. 2007) is added to fit the marginally rising shape above 4 keV. We fix the inclination of the reflector at 30°, and fix the spectral index of the hard Comptonization component at 2.26 (see Section 4). We correct for extinction by a Galactic column density of $N_{\rm H} = 1.91 \times 10^{20}\,{\rm cm}^{-2}$ (Kalberla et al. 2005). We also allow for intrinsic extinction in the host galaxy. This gives a best fit around $N_{\rm H} = 2 \times 10^{20}\,{\rm cm}^{-2}$ at $z = 0.0811$ (`zwabs` model, Morrison & McCammon 1983). Both Galactic and intrinsic reddening are assumed to follow the standard dust-to-gas conversion formula of $E(B-V) = 1.7 \times 10^{-22} N_{\rm H}$ (Bessell 1991) and modelled by `the redden` and `zredden` model (Cardelli, Clayton & Mathis 1989) in XSPEC.

The far-UV *GALEX* points lie well on the expected disc spectrum from OPTXAGNF, but the optical and near UV points display a curvature similar to that from host galaxy emission. The SDSS images show that the host galaxy of RX1140 is of an Sc type galaxy. Therefore, we select an Sc galaxy template from the SWIRE library (Polletta et al. 2007) and incorporate this into our XSPEC model. A normalizing constant is added to account for the different star formation rate and stellar mass of the template galaxy, and the host galaxy of RX1140. An additional normalization offset is allowed between the *UKIDSS* and SDSS UGRIZ photometric points due to their different aperture sizes sampling different amounts of the host galaxy. Both these normalization factors are well constrained by the data. The shape of *UKIDSS* JYHK points match well to both the template and the SDSS UGRIZ points after a scaling of 76 per cent.

Fig. 7 shows the extinction/reddening/aperture corrected data (coloured points, compared to the observed data points in grey) and the best-fitting SED model. The fit statistic is not good (reduced $\chi^2 = 982/330$), but this is mainly due to the small error bars of the photometric points in the optical/UV band.

However, the best-fitting BH mass is $9.6 \times 10^6\,{\rm M}_\odot$. This is almost an order of magnitude higher than the BH mass estimated from optical spectroscopy and reverberation (Greene et al. 2008; Rafter et al. 2011). Using this higher BH mass, the Eddington ratio is correspondingly low, $L/L_{\rm Edd} = 0.17$, which is in conflict with the classification of this object as an NLS1. But the NLS1 classification is supported by the steep X-ray spectrum, and by the OPTXAGNF coronal radius of $\sim 15 R_{\rm g}$, consistent with typical values for NLS1 (J12b, D12).

We test how robustly the SED modelling constrains BH mass by fitting pure disc models down to $15 R_{\rm g}$ (dashed lines) to the UV points for masses of 1.5×10^5 (blue: $L/L_{\rm Edd} = 400$), $1.0 \times 10^6\,{\rm M}_\odot$ (orange: $L/L_{\rm Edd} = 10$) and $1.0 \times 10^7\,{\rm M}_\odot$ (red: $L/L_{\rm Edd} = 0.17$ as before. The red solid line shows the previous best fit. These disc components all give optical fluxes at 5100 Å which match the observed variable flux (Rafter et al. 2011). However, all the reasonable BH masses overpredict the observed X-ray emission by factors of 10–100 (Fig. 8a). Allowing the disc to extend down to $6 R_{\rm g}$ for a non-rotating BH, or $1.2 R_{\rm g}$ for a maximally spinning BH, would make this discrepancy even worse, see Done et al. (2013).

In Fig. 8b, we use the same range of BH masses, but now the aim is to fit the X-ray spectrum, and extrapolate the model to lower energies. The model with a $10^7\,{\rm M}_\odot$ (red curve) can fit the far-UV (and variable optical) data, whereas the model for the 10^6 and $1.5 \times 10^5\,{\rm M}_\odot$ BH masses underpredict the disc continuum by a factor of 10–50, as the peak of the disc spectrum shifts into the soft X-ray band, and its contribution to the UV and optical emission decreases.

The above tests suggest that the broad-band SED can provide strong constraints to the physical model and relevant parameters, especially the BH mass. We discuss this in more detail in the next section.

6 DISCUSSION

6.1 BH mass estimates

Section 1 summarized previous BH mass estimates for RX1140 from RM technique and H β line width. All previous BH masses based on optical spectra report RX1140 to be an IMBH with $M \lesssim 10^6\,{\rm M}_\odot$.

The X-ray variability power spectra also strongly support such a BH low mass, with no observed high-frequency break on time-scales longer than 500 s (see Fig. 2). This means that the total excess variance, $\sigma^2_{\rm rms}$, is high. We include our new data on the M-$\sigma^2_{\rm rms}$ relation (Miniutti et al. 2009; Zhou et al. 2010; Ponti et al. 2012). Fig. 9 shows the reverberation mapped subsample of objects from Ponti et al. (2012), where $\sigma^2_{\rm rms}$ values were calculated from 40 ks light curves in the 2–10 keV band. For RX1140, $\sigma_{\rm rms} = 0.11 \pm 0.04$ in Obs-1 and 0.12 ± 0.08 in Obs-2. Obs-3 gives similar $\sigma^2_{\rm rms}$ as Obs-1 but with bigger uncertainties due to worse signal to noise. The mass inferred from the linear regression line is $1.25 \times 10^6\,{\rm M}_\odot$. A $10^7\,{\rm M}_\odot$ BH mass lies outside the 2σ region, but any BH mass within 3×10^5–$3.0 \times 10^6\,{\rm M}_\odot$ is consistent with the relation (see also Ludlam et al. 2015).

6.2 The SED and mass accretion rate

The BH mass estimate discussed in the previous section highlights the inconsistency between the BH mass derived from the SED models of $\sim 10^7\,{\rm M}_\odot$, and all other determination methods which give $10^6\,{\rm M}_\odot$. For a BH mass of $10^6\,{\rm M}_\odot$, the SED models can either fit the optical/UV flux from the AGN, but then it overpredicts the X-rays (Fig. 8a), or the model can fit the X-rays, but it underpredicts the optical/UV (Fig. 8b). Given that the fraction of optical/UV flux attributed to the AGN is constrained by the observed variability (Rafter et al. 2011), then this requires that the $10^6\,{\rm M}_\odot$ disc fit in Fig. 8 a correctly describes the outer disc, with a derived $L/L_{\rm Edd} = 10$. This estimate is substantially super-Eddington, so there could be substantial energy loss via optically thick advection and/or winds from the inner disc.

In the advection case, part of the energy is swept along with the accretion flow into the BH rather than being emitted as radiation. In the disc wind case, the mass-loss from winds reduces the mass accretion rate in the inner disc, thereby reducing the amount of gravitational energy emitted as radiation. The model used to fit

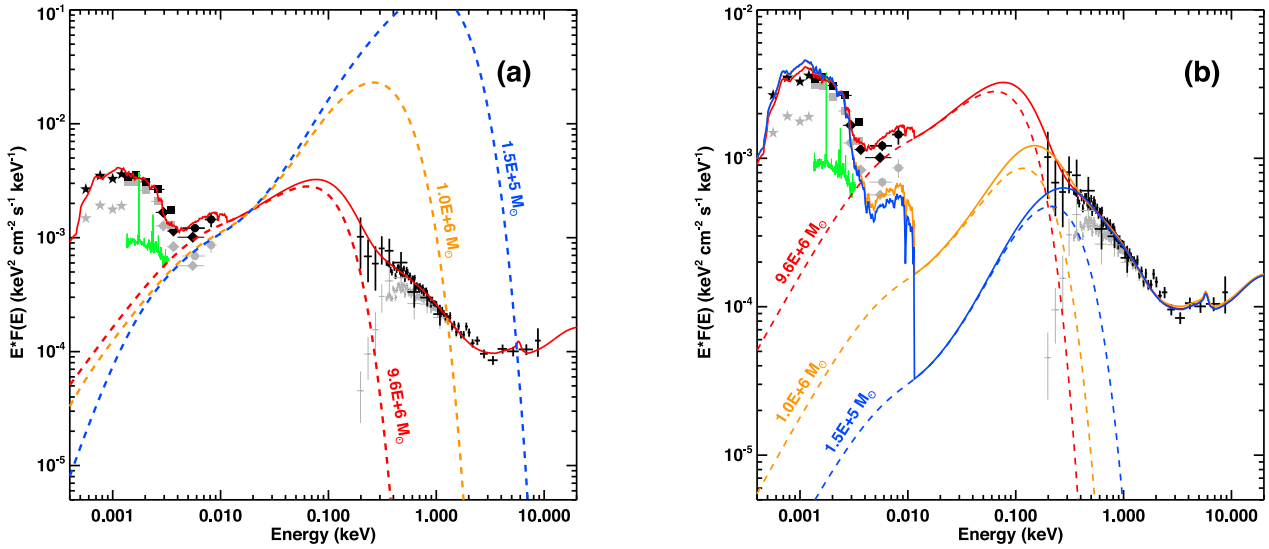

Figure 8. Broad-band SED fitting is similar as in Fig. 7, but with different BH masses: $M = 9.6 \times 10^6\,M_\odot$ (red), $1.0 \times 10^6\,M_\odot$ (orange), $1.5 \times 10^5\,M_\odot$ (blue). In Panel a, the models primarily fit the UV points and have $L/L_{\rm Edd} = 0.17$, 10 and 400, respectively, for disc emission outside 15 $R_{\rm g}$ (see Section 5.2). In Panel b, the models tend to primarily fit the X-ray spectra and have $L/L_{\rm Edd} = 0.17$, 0.56 and 2, respectively. Solid lines are the total models, while dashed lines are the disc components.

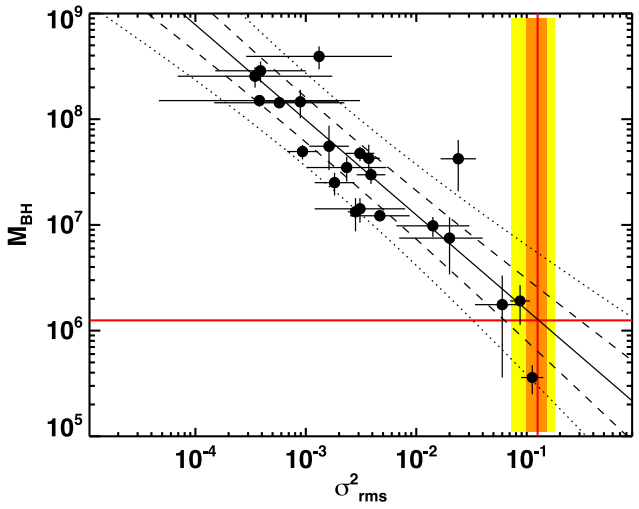

Figure 9. M–$\sigma^2_{\rm rms}$ relation formed by the RM sample, where $\sigma^2_{\rm rms}$ is the excess variance of 2–10 keV for 40 ks time-scale. $\sigma^2_{\rm rms}$ values are taken from Ponti et al. (2012), the RM masses are taken from Peterson et al. (2004, 2005), Denney et al. (2006) and Du et al. (2014). The black solid line is the regression line assuming $\sigma^2_{\rm rms}$ as an independent variable. Dashed and dotted lines show the $\pm1\sigma$ and $\pm2\sigma$ confidence ranges for the new observations. The red vertical line indicates the mean $\sigma^2_{\rm rms}$ for RX1140, with $\pm1\sigma$ intervals determined from Obs-1 (orange) and Obs-2 (yellow). The horizontal red line indicates the BH mass of RX1140 predicted by the regression line.

the SED assumes that the situation is sub-Eddington, and therefore that neither of these two processes is important. It follows that this conclusion may no longer be valid for super-Eddington objects, such as may be the case for RX1140 (orange and blue lines in Fig. 8a).

The degree of energy losses due to winds/advection can be estimated from the best-fitting SED model. The parameters of $M = 10^7\,M_\odot$, $L/L_{\rm Edd} = 0.17$ give $L_{\rm bol} \sim 2 \times 10^{44}$ ergs cm^{-2} s^{-1}, which is close to the Eddington limit for the most probable BH mass of $10^6\,M_\odot$. This is in support of the proposal of Wang et al. (2014) that super-Eddington BHs have a total luminosity which saturates around the Eddington limit.

However, RX1140 has another unusual feature. It exhibits strong optical variability, as seen in the RM campaign of Rafter et al. (2011). The majority of NLS1 show less optical variability than the broad-line Seyferts (e.g. Ai et al. 2013, but see Kelly et al. 2013). This is somewhat surprising in view of their higher X-ray variability (e.g. Ponti et al. 2012). The unusually strong optical variability in RX1140 could indicate that some of the X-rays are reprocessed within a large scale wind. If so the models above in Fig. 8a, which require only disc emission to fit the optical, may be overestimating the mass accretion rate. None the less, there must still be sufficient X-ray emission to power an additional optical component. The X-ray model fit based on $10^6\,M_\odot$ shown in Fig. 8 b has an X-ray peak which has similar νL_ν to that required to explain the far-UV emission. So this model with $L/L_{\rm Edd} = 0.56$ would require that almost all the X-rays are reprocessed. A more likely reprocessing fraction of 10–50 per cent would require a higher Eddington ratio of 1–5. So perhaps the most plausible model is a combination of the two $10^6\,M_\odot$ models in Fig. 8 a and b, where the X-ray emission is partly suppressed by wind/advection energy losses, and the optical emission is correspondingly enhanced by reprocessing in the wind.

6.3 Super-Eddington accretion flow

We note that if winds and advection do play a significant role, it is curious that the X-ray spectrum and variability properties, including the lack of absorption signatures in the X-ray spectra, are not more noticeably different from the other well-studied NLS1s, such as PG 1244+026, RE J1034+396 and RX J0136.9−3510 (e.g. Jin et al. 2009, 2013, Middleton et al. 2009). This raises the possibility that these sources are likewise super-Eddington. PG 1244+026 has an SED which is acceptably well fitted by a $10^7\,M_\odot$ BH accreting at about $L_{\rm Edd}$ (Done et al. 2013). This SED has a distinct outer disc spectral shape in the optical/UV (e.g. Done et al. 2013), which constrains $(M\dot{M})^{2/3} \propto (M^2 L/L_{\rm Edd})^{2/3}$. Reducing the BH mass by

a factor of 4 to 2.5 $\times$ 10^6 $M_\odot$ i.e. removing the Marconi et al. (2008) radiation pressure correction to the H β line velocity width, then requires $L/L_{\rm Edd} = 16$, i.e. very super-Eddington (see Done & Jin 2015), which would then invalidate the BH spin determination described in Done et al. (2013).

If the majority of all NLS1s are super-Eddington, but the typical broad-line Seyfert 1's have $L/L_{\rm Edd} \sim 0.05$–0.2, then this implies a distinct bimodal (or a very long tail), mass accretion rate distribution. Also, such high-energy losses due to advection/winds are probably not seen in the majority of ultraluminous X-ray sources (e.g. Sutton et al. 2015), although they may be present in the more extreme sources discussed by Gladstone, Roberts & Done (2009). The current data suggest that most of these sources represent moderately super-Eddington flows on to stellar mass BHs with masses of around 30 $M_\odot$ compared with those with $\sim$10 $M_\odot$ seen in our Galaxy, due to their lower metallicity resulting in less mass-loss from winds: Zampieri & Roberts (2009). Theoretical models predict rather high efficiency for these flows (Jiang, Stone & Davis 2014, but see also Sądowski et al. 2015 who report lower efficiency). Clearly there remain many aspects of super-Eddington accretion flows which are not yet understood.

7 SUMMARY

In this paper, we use new *XMM–Newton* data from one of the lowest mass AGN known as a means to better understand the nature of the soft X-ray excess, and how this relates to its broad-band SED. The mass from H β line width (uncorrected for radiation pressure: Marconi et al. 2008), upper limit from RM and fast X-ray variability are all consistent with a BH mass of 10^6 $M_\odot$. This, together with a steep 2–10 keV X-ray spectrum, and even steeper soft X-ray emission in this object make it a clear member of the 'typical' NLS1 class of AGN, having low BH mass and a high accretion rate.

We fit the time-averaged X-ray data together with the covariance spectra of the fast variability, and show that both low-temperature Comptonization and highly smeared, ionized reflection models can fit the data, but that both require an additional component at the lowest X-ray energies which we interpret as arising from the inner disc. However, the RMS, lag and coherence spectra all suggest a break in variability properties between the soft and hard X-ray bands, which is not consistent with the reflection model. Instead, these characteristics support the low-temperature Comptonization model as this component does not extend into the 2–10 keV band. All these properties are similar to other 'typical' NLS1s such as PG 1244+026 (Jin et al. 2013), RE J1934+396 (Middleton et al. 2009) and RX J0136.9−3510 (Jin et al. 2009).

However, when considering the X-ray data in the context of the broad-band SED an enigma is revealed. The far-UV and variable optical flux require an outer disc which has $L/L_{\rm Edd} \sim 10$ for an assumed BH mass of 10^6 $M_\odot$. But the model then far overpredicts the soft X-ray emission for standard efficiency, even assuming zero spin for the BH. This could be explained if a substantial amount of energy is lost via advection and/or winds. Other alternatives are if the BH mass is underestimated by a factor of 10, or the variable optical flux does not predominantly emerge from the outer accretion disc. However, both of these explanations seem very unlikely. If RX J1140 is indeed super Eddington and other similar NLS1 are also, this would remove the requirement for low spin in these objects (Done et al. 2013). Another consequence is that it would be then be unlikely that the geometry of these NLS1s could be well represented by a flat disc, as is used in reverberation studies. Clearly, more work is needed before we can claim that we have a picture that is simultaneously consistent with the variability, SED and back hole mass.

ACKNOWLEDGEMENTS

We thank our referee for providing valuable comments and suggestions which has clarified our discussion and improved this paper. This work is based on observations obtained using *XMM–Newton*, an ESA science mission with instruments and contributions directly funded by ESA member states and NASA. This work makes use of data from the SDSS, whose funding is provided by the Alfred P. Sloan Foundation, the participating institutions, the National Science Foundation, the US Department of Energy, the National Aeronautics and Space Administration, the Japanese Monbukagakusho, the Max Planck Society, and the Higher Education Funding Council for England. We have made use of the *ROSAT* Data Archive of the Max-Planck-Institut für extraterrestrische Physik (MPE) at Garching, Germany.

REFERENCES

Ai Y. L., Yuan W., Zhou H. Y., Wang T. G., Zhang S. H., 2011, ApJ, 727, 31
Ai Y. L., Yuan W., Zhou H., Wang T. G., Dong X. B., Wang J. G., Lu H. L., 2013, AJ, 145, 90
Arnaud K. A., 1996, in Jacoby G. H., Barnes J., eds, ASP Conf. Ser. Vol. 101, Astronomical Data Analysis Software and Systems V. Astron. Soc. Pac., San Francisco, p. 17
Barth A. J., Ho L. C., Rutledge R. E., Sargent W. L. W., 2004, ApJ, 607, 90
Baskin A., Laor A., Stern J., 2014, MNRAS, 438, 604
Bentz M. C. et al., 2006, ApJ, 651, 775
Bentz M. C., Peterson B. M., Netzer H., Pogge R. W., Vestergaard M., 2009a, ApJ, 697, 160
Bentz M. C. et al., 2009b, ApJ, 705, 199
Bessell M. S., 1991, A&A, 242, L17
Boroson T. A., 2002, ApJ, 565, 78
Boroson T. A., Green R. F., 1992, ApJS, 80, 109
Cardelli J. A., Clayton G. C., Mathis J. S., 1989, ApJ, 345, 245
Davis S. W., Laor A., 2011, ApJ, 728, 98
Denney K. D. et al., 2006, ApJ, 653, 152
Denney K. D. et al., 2010, ApJ, 721, 715
Done C., Jin C., 2015, MNRAS, preprint (arXiv:1506.04547)
Done C., Davis S. W., Jin C., Blaes O., Ward M., 2012, MNRAS, 420, 1848 (D12)
Done C., Jin C., Middleton M., Ward M., 2013, MNRAS, 434, 1955
Dong X. et al., 2007, ApJ, 657, 700
Du P. et al., 2014, ApJ, 782, 45
Edelson R., Turner T. J., Pounds K., Vaughan S., Markowitz A., Marshall H., Dobbie P., Warwick R., 2002, ApJ, 568, 610
Elvis M. et al., 1994, ApJS, 95, 1
Fabian A. C., Miniutti G., 2009, in Wiltshire D. L., Visser M., Scott S. M., eds, Kerr Spacetime: Rotating Black Holes in General Relativity. Cambridge Univ. Press, Cambridge, p. 236
Fabian A. C. et al., 2009, Nature, 459, 540
Fabian A. C. et al., 2013, MNRAS, 429, 2917
Fabian A. C., Kara E., Parker M. L., 2014, Suzaku-MAXI 2014: Expanding the Frontiers of the X-ray Universe, p. 279
Filippenko A. V., Ho L. C., 2003, ApJ, 588, 13
Gardner E., Done C., 2015, MNRAS, 448, 2245
Gierliński M., Done C., 2004, MNRAS, 349, L7
Gierliński M., Done C., 2006, MNRAS, 371, L16
Gladstone J. C., Roberts T. P., Done C., 2009, MNRAS, 397, 1836
Greene J. E., Ho L. C., 2004, ApJ, 610, 722
Greene J. E., Ho L. C., 2007, ApJ, 670, 92
Greene J. E., Ho L. C., Barth A. J., 2008, ApJ, 688, 159
Hua X.-M., Titarchuk L., 1995, ApJ, 449, 188

Jiang Y. F., Stone J. M., Davis S. W., 2014, ApJ, 796, 106
Jin C., Done C., Ward M., Gierliński M., Mullaney J., 2009, MNRAS, 398, L16
Jin C., Ward M., Done C., Gelbord J., 2012a, MNRAS, 420, 1825 (J12a)
Jin C., Ward M., Done C., 2012b, MNRAS, 425, 907 (J12b)
Jin C., Done C., Middleton M., Ward M., 2013, MNRAS, 436, 3173
Kalberla P. M. W., Burton W. B., Hartmann D., Arnal E. M., Bajaja E., Morras R., Pöppel W. G. L., 2005, A&A, 440, 775
Kaspi S., Smith P. S., Netzer H., Maoz D., Jannuzi B. T., Giveon U., 2000, ApJ, 533, 631
Kelly B. C., Treu T., Malkan M., Pancoast A., Woo J. H., 2013, ApJ, 779, 187
Kunth D., Sargent W. L. W., Bothun G. D., 1987, AJ, 93, 29
Laor A., 1991, ApJ, 376, 90
Laor A., Fiore F., Elvis M., Wilkes B. J., McDowell J. C., 1997, ApJ, 477, 93
Leighly K. M., 1999, ApJS, 125, 317
Ludlam R. M., Cackett E. M., Gültekin K., Fabian A. C., Gallo L., Miniutti G., 2015, MNRAS, 447, 2112
McHardy I. M., Papadakis I. E., Uttley P., Page M. J., Mason K. O., 2004, MNRAS, 348, 783
Magdziarz P., Blaes O. M., Zdziarski A. A., Johnson W. N., Smith D. A., 1998, MNRAS, 301, 179
Makishima K., Maejima Y., Mitsuda K., Bradt H. V., Remillard R. A., Tuohy I. R., Hoshi R., Nakagawa M., 1986, ApJ, 308, 635
Marconi A., Axon D. J., Maiolino R., Nagao T., Pastorini G., Pietrini P., Robinson A., Torricelli G., 2008, ApJ, 678, 693
Marconi A., Axon D. J., Maiolino R., Nagao T., Pietrini P., Risaliti G., Robinson A., Torricelli G., 2009, ApJ, 698, L103
Markowitz A., Edelson R., Vaughan S., 2003, ApJ, 598, 935
Matt G. et al., 2014, MNRAS, 439, 3016
Middleton M., Done C., Ward M., Gierliński M., Schurch N., 2009, MNRAS, 394, 250
Miniutti G., Ponti G., Greene J. E., Ho L. C., Fabian A. C., Iwasawa K., 2009, MNRAS, 394, 443
Mitsuda K. et al., 1984, PASJ, 36, 741
Morrison R., McCammon D., 1983, ApJ, 270, 119
Nandra K., O'Neill P. M., George I. M., Reeves J. N., 2007, MNRAS, 382, 194
Nowak M. A., Wilms J., Vaughan B. A., Dove J. B., Begelman M. C., 1999, ApJ, 515, 726
Osterbrock D. E., Pogge R. W., 1985, ApJ, 297, 166
Peterson B. M., 1997, An Introduction to Active Galactic Nuclei. Cambridge Univ. Press, Cambridge
Peterson B. M. et al., 2004, ApJ, 613, 682
Peterson B. M. et al., 2005, ApJ, 632, 799
Polletta M. et al., 2007, ApJ, 663, 81
Ponti G., Papadakis I., Bianchi S., Guainazzi M., Matt G., Uttley P., Bonilla N. F., 2012, A&A, 542, A83
Rafter S. E., Kaspi S., Behar E., Kollatschny W., Zetzl M., 2011, ApJ, 741, 66
Schurch N. J., Done C., 2007, MNRAS, 381, 1413
Sutton A. D., Roberts T. P., Gladstone J. C., Walton D. J., 2015, MNRAS, 450, 787
Sądowski A., Narayan R., Tchekhovskoy A., Abarca D., Zhu Y., McKinney J. C., 2015, MNRAS, 447, 49
Titarchuk L., 1994, ApJ, 434, 570
Titarchuk L., Lyubarskij Y., 1995, ApJ, 450, 876
Uttley P., Cackett E. M., Fabian A. C., Kara E., Wilkins D. R., 2014, A&AR, 22, 72
Vaughan S., Edelson R., Warwick R. S., Uttley P., 2003, MNRAS, 345, 1271
Wang J. M. et al., 2014, ApJ, 793, 108
Wilkinson T., Uttley P., 2009, MNRAS, 397, 666
Zampieri L., Roberts T. P., 2009, MNRAS, 400, 677
Zdziarski A. A., Johnson W. N., Magdziarz P., 1996, MNRAS, 283, 193
Zhang E. P., Wang J. M., 2006, ApJ, 653, 137
Zhou X. L., Zhang S. N., Wang D. X., Zhu L., 2010, ApJ, 710, 16
Zoghbi A., Fabian A. C., Uttley P., Miniutti G., Gallo L. C., Reynolds C. S., Miller J. M., Ponti G., 2010, MNRAS, 401, 2419
Życki P. T., Done C., Smith D. A., 1999, MNRAS, 309, 561

This paper has been typeset from a TEX/LATEX file prepared by the author.